J. Fluid Mech. (2017), *vol.* 824, *pp.* 866–885. © Cambridge University Press 2017
doi:10.1017/jfm.2017.306

Drops bouncing off macro-textured superhydrophobic surfaces

Ali Mazloomi Moqaddam[1], Shyam S. Chikatamarla[1] and Iliya V. Karlin[1,†]

[1]Aerothermochemistry and Combustion Systems Laboratory, Department of Mechanical and Process Engineering, ETH Zurich, 8092 Zurich, Switzerland

(Received 9 August 2016; revised 3 March 2017; accepted 5 May 2017; first published online 13 July 2017)

Recent experiments with droplets impacting macro-textured superhydrophobic surfaces revealed new regimes of bouncing with a remarkable reduction of the contact time. Here we present a comprehensive numerical study that reveals the physics behind these new bouncing regimes and quantifies the roles played by various external and internal forces. For the first time, accurate three-dimensional simulations involving realistic macro-textured surfaces are performed. After demonstrating that simulations reproduce experiments in a quantitative manner, the study is focused on analysing the flow situations beyond current experiments. We show that the experimentally observed reduction of contact time extends to higher Weber numbers, and analyse the role played by the texture density. Moreover, we report a nonlinear behaviour of the contact time with the increase of the Weber number for imperfectly coated textures, and study the impact on tilted surfaces in a wide range of Weber numbers. Finally, we present novel energy analysis techniques that elaborate and quantify the interplay between the kinetic and surface energy, and the role played by the dissipation for various Weber numbers.

Key words: contact lines, drops, multiphase flow

1. Introduction

Impact of liquid drops on solid surfaces is a fascinating fluidics problem whose complexity derives from the possible coexistence of a variety of phenomena occurring at multiple temporal and spatial event scales (Yarin 2006; Roisman, Berberović & Tropea 2009; Roisman 2009). These include but are not limited to splash (Xu, Zhang & Nagel 2005; Xu 2007; Mani, Mandre & Brenner 2010; Mandre & Brenner 2012; Riboux & Gordillo 2014), phase-change-induced surface levitation (Wachters & Westerling 1966; Biance, Clanet & Quéré 2003; Tran *et al.* 2012, 2013; Antonini *et al.* 2013*a*), skating (Kolinski *et al.* 2012), rebounding (Richard, Clanet & Quéré 2002; Antonini *et al.* 2013*b*; Bird *et al.* 2013; Liu *et al.* 2014; De Ruiter *et al.* 2015), prompt tumbling-rebound (Antonini *et al.* 2016) and the trampoline effect (Schutzius *et al.* 2015).

Surfaces with special wetting properties have profound implications in engineering including power generation, transportation, water desalination, oil and gas production

† Email address for correspondence: karlin@lav.mavt.ethz.ch

and microelectronics thermal management. Particularly interesting are surfaces with extreme wetting properties, which are efficient at either repelling (hydrophobic) or attracting liquids (hydrophilic) such as water and oils but can also prevent formation of biofilms or ice (Rykaczewski *et al.* 2012). The degree of surface wetting, typically measured by a drop's equilibrium contact angle, depends on the balance of the products of corresponding interfacial surface areas and surface energies. From a theoretical perspective, the contact angle of a liquid interacting with a flat solid is predicted by Young's equation. However, in order to achieve extreme wetting properties, the interface between the droplet and the substrate must be structured and often contains an additional gas or liquid phase (Rykaczewski *et al.* 2012). For example, nano- and/or microscale roughening of a flat hydrophobic substrate yields a superhydrophobic surface (SHS) through trapping gas. SHS are characterized by high contact angle $\theta \geqslant 150^\circ$ and negligible contact angle hysteresis. Drop repellence by hydrophobic and superhydrophobic surfaces is an area of active research (Rein 1993; Richard *et al.* 2002; Blossey 2003; Okumura *et al.* 2003; Yarin 2006; Tuteja *et al.* 2007; Jung *et al.* 2012; Bird *et al.* 2013; Liu *et al.* 2014, 2015*a*; Gauthier *et al.* 2015; Schutzius *et al.* 2015).

The time during which the drop stays in a contact with the solid after impact is termed the contact time (or rebound time). Minimization of contact time is important for a rational design of hierarchically structured surfaces and has been the focus of recent studies (Richard *et al.* 2002; Bird *et al.* 2013; Liu *et al.* 2014, 2015*a*; Gauthier *et al.* 2015; Schutzius *et al.* 2015). Richard, Clanet and Quéré (Richard *et al.* 2002) found that the conventional mechanism of rebound on macroscopically flat superhydrophobic surfaces (impact–spread–recoil–rebound, (Richard & Quéré 2000; Richard *et al.* 2002; Okumura *et al.* 2003; Wang *et al.* 2007)) scales universally with the inertia–capillarity time,

$$\tau = \sqrt{\frac{\rho_l R_0^3}{\sigma}}, \tag{1.1}$$

with ρ_l, R_0 and σ the liquid density, drop radius and surface tension, respectively. This scaling, $t_{contact}/\tau \approx 2.2 \pm 0.3$, is notably independent on the drop kinetic energy and holds in a range of Weber numbers (Richard *et al.* 2002),

$$We = \frac{\rho_l R_0 U_0^2}{\sigma}, \tag{1.2}$$

where U_0 is the impact velocity. However, (Bird *et al.* 2013) demonstrated that by adding a macro-texture (few hundred micrometres) as a ridge on the flat surface, the contact time reduces by approximately 37 %. Recently, (Liu *et al.* 2014) demonstrated that impact on a flat surface decorated with a lattice of sufficiently tall (almost a millimetre) tapered posts with a nanoscale superhydrophobic coating results in an unconventional mechanism where the drop rebounds even before the retraction takes place. Because of the flattened droplet shape at rebound, this phenomenon was referred to as pancake bouncing. A spectacular reduction in contact time by a factor of four was reported. Further experimental studies of similar macro-textures can be found in Gauthier *et al.* (2015), Liu *et al.* (2015*a*).

Although pancake bouncing was shown to reduce the contact time significantly, questions remain regarding the physics behind the phenomenon, including the role played by surface energy, viscous dissipation and the influence of air pockets that

might be trapped between the droplet and the surface texture. Also a parametric study including the dependence on the texture geometry, quality of coating, velocity of the drop etc. can help to understand the limits and optimizations of the macro-texture proposed in Liu *et al.* (2014).

Such detailed analysis and information regarding the complex droplet shape and its deformation can be made possible through simulations. To this end, simulations of Moevius *et al.* (2014) were able to capture pancake bouncing in a qualitative manner. However, due to limitations of the lattice Boltzmann model used in Moevius *et al.* (2014), a quantitative comparison was restrictive. First, only a quasi-three-dimensional simulation was performed (cylindrical droplet instead of spherical) and only square posts rather than the tapered posts were considered. Another limitation was due to the high relative density of the gas phase which precluded the study of the actual surface geometry.

In this paper, we report a comprehensive simulation study of the pancake bouncing effect and outline a new energy analysis technique that could reveal the interplay between kinetic, surface and viscous forces that influence droplet–wall interactions. The recently introduced entropic lattice Boltzmann method (ELBM) for two-phase flows (Mazloomi Moqaddam, Chikatamarla & Karlin 2015*b*) is free of the aforementioned limitations and enables us to consider complex texture with a realistic geometry. First, validity and accuracy of the ELBM is established through comparison to recent experiments on pancake bouncing on SHS macro-textures (Liu *et al.* 2014) and interaction of a droplet with a flat surface. After that, a detailed parametric study is conducted by varying the geometry of macro-texture and the contact angle on the substrate. Analysis of various forces and energies acting during the collision process is also provided. It is important to note that the model used here is free of tuning parameters and case-based modelling. The simulation algorithm remains the same as in previous studies of binary droplets collisions, interaction with flat or complex walls and tumbling rebound from inclined sublimating slope (Mazloomi Moqaddam, Chikatamarla & Karlin 2015*a*; Mazloomi Moqaddam *et al.* 2015*b*; Mazloomi Moqaddam, Chikatamarla & Karlin 2015*c*, 2016; Antonini *et al.* 2016). Such accurate and reliable simulations combined with novel analysis techniques can uncover the physics behind these droplet–wall interactions and lead to the design, optimization and also discovery of new surfaces.

The outline of the paper is as follows: in § 2 we briefly explain our numerical model. Main § 3 opens with the geometry of complex macro-texture and description of physical parameters used in the simulation (§ 3.1). In § 3.2, simulations are validated against experiments on the flat (Bird *et al.* 2013) and macro-textured SHS of Liu *et al.* (2014). The pancake bouncing regime is further studied at higher Weber numbers in § 3.3. Influence of density of texture on the contact time reduction is studied through simulation and scaling analysis in § 3.4, while in § 3.5 the nonlinear effect of coating quality is revealed. In § 3.6, energy analysis is reported. Simulation of the impact on a tilted macro-structure is reported in § 3.7. Finally, the paper is summarized in § 4.

2. Simulation method

We use the ELBM for two-phase flows (Mazloomi Moqaddam *et al.* 2015*b*). The method was already discussed in detail elsewhere (Mazloomi Moqaddam *et al.* 2015*b*,*c*, 2016); a summary is given below. The ELBM equation for the populations $f_i(\boldsymbol{x}, t)$ of the discrete velocities $\boldsymbol{v}_i$, $i = 1, \ldots, N$, reads,

$$f_i(\boldsymbol{x} + \boldsymbol{v}_i\delta t, t + \delta t) = f_i(\boldsymbol{x}, t) + \alpha\beta[f_i^{eq}(\rho, \boldsymbol{u}) - f_i(\boldsymbol{x}, t)] + [f_i^{eq}(\rho, \boldsymbol{u} + \delta\boldsymbol{u}) - f_i^{eq}(\rho, \boldsymbol{u})]. \quad (2.1)$$

We use the lattice with $N = 27$ discrete velocities $\boldsymbol{v}_i = (v_{ix}, v_{iy}, v_{iz})$ where $v_{i\xi} = \{\pm 1, 0\}$. The equilibrium populations f_i^{eq} minimize the discrete entropy function $H = \sum_{i=1}^{N} f_i \ln(f_i/W_i)$ under fixed density and momentum, $\{\rho, \rho\boldsymbol{u}\} = \sum_{i=1}^{N}\{1, \boldsymbol{v}_i\}\{f_i^{eq}\}$, where W_i are the lattice weights (Karlin, Ferrante & Öttinger 1999; Ansumali, Karlin & Öttinger 2003; Chikatamarla, Ansumali & Karlin 2006). Parameter $0 < \beta < 1$ is fixed by the kinematic viscosity ν through $\nu = c_s^2\delta t[1/(2\beta) - 1/2]$. Here $c_s = \delta x/(\sqrt{3}\delta t)$ is the lattice speed of sound; lattice units $\delta x = \delta t = 1$ are used. The relaxation parameter α is computed at each lattice site and at every time step from the entropy balance condition (Karlin *et al.* 1999). The latter provides numerical stability without compromising on the accuracy thus significantly reducing the grid requirements for the simulation at high Weber and Reynolds numbers.

Furthermore, in (2.1), the last term implements the phase separation and fluid–solid interaction through evaluation of the flow velocity increment, $\delta\boldsymbol{u} = (\boldsymbol{F}/\rho)\delta t$, with the force $\boldsymbol{F} = \boldsymbol{F}_f + \boldsymbol{F}_s$. The mean-field force $\boldsymbol{F}_f = \boldsymbol{\nabla}\cdot(\rho c_s^2\boldsymbol{I} - \boldsymbol{P})$ implements Korteweg's stress (Rowlinson & Widom 1982; Korteweg 1901),

$$\boldsymbol{P} = \left(p - \kappa\rho\nabla^2\rho - \frac{\kappa}{2}|\boldsymbol{\nabla}\rho|^2\right)\boldsymbol{I} + \kappa(\boldsymbol{\nabla}\rho)\otimes(\boldsymbol{\nabla}\rho), \tag{2.2}$$

where κ is the coefficient which controls the surface tension, $\boldsymbol{I}$ is unit tensor and p is the equation of state; the Peng–Robinson form is used for the latter (Mazloomi Moqaddam *et al.* 2015*b*,*c*, 2016). Interaction between the fluid and the solid surface is introduced with the help of a force $\boldsymbol{F}_s$,

$$\boldsymbol{F}_s(\boldsymbol{x}, t) = \kappa_w\rho(\boldsymbol{x}, t)\sum_{i=1}^{N} w_i s(\boldsymbol{x} + \boldsymbol{v}_i\delta t)\boldsymbol{v}_i, \tag{2.3}$$

where the parameter κ_w reflects the intensity of the fluid–solid interaction. By adjusting κ_w, solid surfaces with different wetting can be modelled. In (2.3), $s(\boldsymbol{x} + \boldsymbol{v}_i\delta t)$ is an indicator function that is equal to one for the solid domain nodes and is equal to zero otherwise; w_i are appropriately chosen weights (Yuan & Schaefer 2006; Mazloomi Moqaddam *et al.* 2015*c*). Following Mazloomi Moqaddam *et al.* (2015*c*), the equilibrium contact angle is set in accord with the Young–Laplace equation by choosing coefficient κ_w in (2.3). In the simulations presented below, the equilibrium contact angle was set at $\theta = 165°$, corresponding to $\kappa_w = -0.1475$ in (2.3). Since for the SHS the contact angle hysteresis is small (∼2°–3°), the advancing and receding contact angles are not explicitly modelled. Also, the numerical simulations presented below demonstrate that this affects the dynamics of drop impact on neither flat nor macro-textured SHS and that experimentally observed results are captured both qualitatively and quantitatively.

3. Results

3.1. *Geometry and simulation parameters*

The set-up of the three-dimensional simulations is sketched in figure 1. A droplet of radius R_0 is placed above the surface in equilibrium with the vapour. A uniform downward velocity is imposed on the drop while surrounding vapour is initialized with zero velocity. Initially the drop is sufficiently elevated to allow the liquid–vapour interface to equilibrate before the impact. No gravity is considered in the simulations due to the small time scales involved. All simulations, unless otherwise stated, were

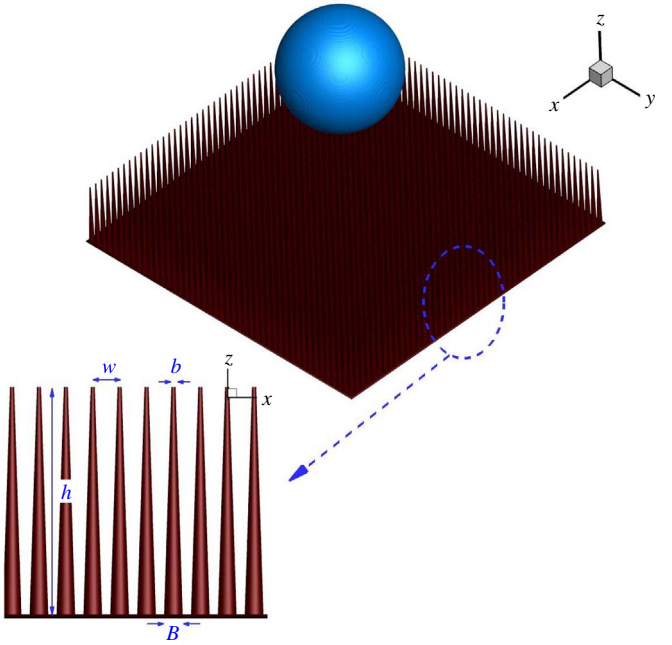

FIGURE 1. (Colour online) Simulation set-up. The texture is represented as a surface decorated with a lattice of tapered posts. The posts are represented by right conical frustums with the base diameters b and B; w is the centre-to-centre spacing and h is the height of the posts.

run on computational domain of $6R_0 \times 6R_0 \times 6R_0$. Parameters of the simulated fluid are the same as the ones employed for investigation of droplets collisions (Mazloomi Moqaddam *et al.* 2016) and the droplet–surface interactions (Mazloomi Moqaddam *et al.* 2015*c*): $\rho_l = 7.82$ (liquid density), $\rho_v = 0.071$ (vapour density), $\sigma = 0.353$ (surface tension, corresponding to $\kappa = 0.00468$ in (2.2)) and $\mu_v = 0.01$ (vapour dynamic viscosity); all are in lattice units (see below the match to physical units). The impact velocity was computed in accord with the Weber number $We = \rho_l R_0 U_0^2/\sigma$, and the range $6 \leqslant We \leqslant 150$ was studied. The dynamic viscosity of the droplet was fixed at $\mu_l = 0.415$ corresponding to Ohnesorge number $Oh = 0.025$ ($Oh = \mu_l/\sqrt{\rho_l \sigma R_0}$). This corresponds to a range of Reynolds number $Re = \sqrt{We}/Oh$ as $98 \leqslant Re \leqslant 490$.

A comment on the parameters of the simulated liquid and those used by the experiment (Liu *et al.* 2014) (water) is in order. The density contrast $\rho_l/\rho_v \approx 100$ and the Ohnesorge number $Oh = 0.025$ used in the ELBM simulations were shown before to be sufficient to recover the pertinent flow dynamics of colliding droplets and impacts on flat surfaces (Mazloomi Moqaddam *et al.* 2015*c*, 2016). The density contrast for water is an order of magnitude higher, whereas the Ohnesorge number is an order of magnitude lower than those of the simulation ($Oh \approx 0.003$ for water). Nevertheless, similar to previously studied cases, we expect the essential dynamics to be captured correctly also in the present simulations with complex textures since the vapour state is too light to influence the liquid (Mazloomi Moqaddam *et al.* 2015*c*, 2016). Further evidence is provided below by comparing ELBM simulations with experiments.

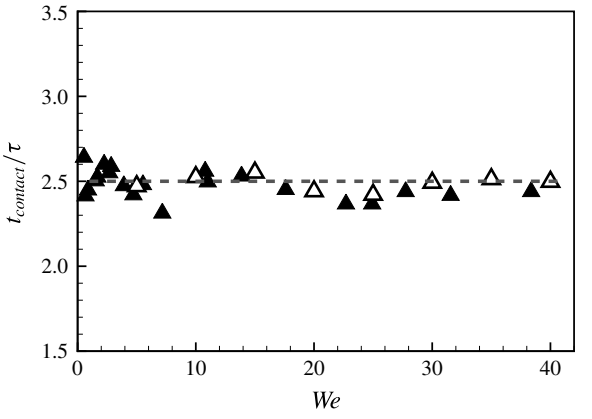

FIGURE 2. Contact time on a flat superhydrophobic surface with the contact angle $\theta = 161°$ as a function of Weber number. Open symbols: ELBM simulations; solid symbols: experiment (Gauthier *et al.* 2015). Dashed line: $t_{contact}/\tau = 2.5$.

The structure of the substrate is a square lattice of tapered posts placed uniformly with the centre-to-centre spacing w on a flat plate. Each post is modelled as a right conical frustum of the height h, with the smaller and larger base diameters b and B, respectively. The droplet radius R_0 is the input of the simulations while the rest of the geometry matches the experiment (Liu *et al.* 2014): $R_0/h = 1.8$ (droplet radius to post height), $b/B \approx 0.28$ and $b = B - 2h\tan\varphi$ ($\varphi = 2.6°$ is the apex angle (Liu *et al.* 2014)). We introduce the density of the texture (DoT) $\Lambda = R_0/w$ (parameter Λ reflects the relative number of posts 'seen' by the droplet at impact). The spacing between the posts was chosen to reproduce $\Lambda_{exp} \approx 7.25$ (Liu *et al.* 2014) in the simulations of § 3.2 below. Both the surface of the conical frustum and the supporting flat plate are considered SHS with a contact angle $\theta = 165°$.

Finally, in order to convert lattice time t_{LB} into seconds, we first compute the inertia–capillary time $\tau_{LB} = \sqrt{\rho_l R_0^3/\sigma}$ using the density, droplet radius and surface tension in lattice units. Next, τ is extracted from the experimental data and the reduced time for both the experiment and the simulation are matched, $t_{LB}/\tau_{LB} = t/\tau$. Thus, given t_{LB} (the number of time steps), we uniquely obtain the corresponding physical time $t = (\tau/\tau_{LB})t_{LB}$. A droplet radius of $R_0 = 100$ grid units was used unless stated otherwise. All simulations were checked for grid convergence using $R_0 = 100$ and lower; only the highest resolution results are reported here.

3.2. *Validation with experimental data*

In this section we validate the simulations with published data from experiments (Liu *et al.* 2014; Gauthier *et al.* 2015). For a flat SHS, it was shown in Richard *et al.* (2002) that the contact time $t_{contact}$ is independent of Weber number in a wide range and can be scaled with the inertial–capillary time scale: $t_{contact}/\tau \approx 2.5$. Figure 2 reports the variation of contact time on the flat SHS for a range of Weber numbers; simulation results agree well with the experiment (Gauthier *et al.* 2015). In figure 3, the history of the drop spread on a flat SHS at $We = 26.6$ is reported. Excellent agreement between results obtained by numerical simulations and experimental observations reported in Bird *et al.* (2013) is evident from figure 3.

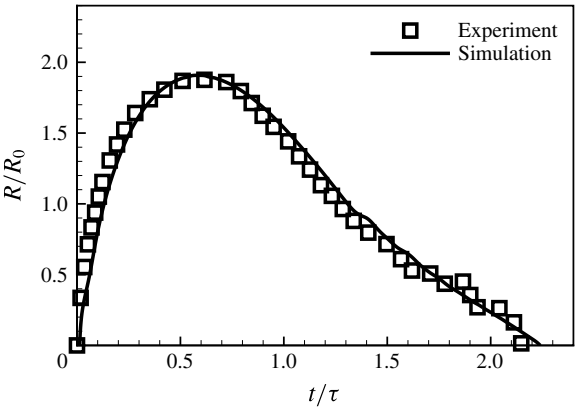

FIGURE 3. Lateral expansion of a water drop impacting on a flat superhydrophobic surface at $We = 26.6$ (supplementary movie 1 available at https://doi.org/10.1017/jfm.2017.306). Line: simulation; symbols: experiment (Bird *et al.* 2013).

We note that the flat SHS test validates the use of the Ohnesorge number of $Oh = 0.025$ for the ELBM fluid in the present context. Indeed, as it has been shown by many authors, e.g. Antonini *et al.* (2013*a*), Maitra *et al.* (2014), that the Ohnesorge number takes effect on the contact time at much higher values, $Oh \approx 1$ (i.e. for highly viscous liquids such as glycerol ($Oh \approx 3$) or silicon oil). For $Oh < 0.1$, there is no effect of viscosity during impact on flat surfaces, and thus it is not surprising that the present simulation agrees well with the experiments which use water. We refer to Mazloomi Moqaddam *et al.* (2015*c*) for other comparisons of ELBM with experiments on a flat SHS.

Now we proceed with the textured SHS. Following Liu *et al.* (2014), we introduce characteristic time instances ($t = 0$ corresponds to the time of first contact): $t_{\uparrow}$ is the time at which the texture is fully emptied (emptying time); at t_{max} the drop reaches its maximal lateral extension; $t_{contact}$ is the time at which the drop loses contact with the surface (contact time). Snapshots of a drop impinging on a texture of tapered posts at $We = 14.1$ are shown in figure 4(*a*) along with the images from the experiment (Liu *et al.* 2014). Pancake formation and rebound is clearly seen in the simulation. Simulation results for both the shape of the drop and the characteristic times are in excellent agreement with experimental observations.

Along with the tapered posts texture of figure 1, we simulated a simpler case of rectangular prism posts which was also considered in the experiment of Liu *et al.* (2014). The droplet radius for this simulation was $R_0 = 34$ lattice units. The height of posts h, the posts centre-to-centre spacing, w and the side of the square cross-section b were computed according to the aspect ratios R_0/h, R_0/w and b/h of the experiment (Liu *et al.* 2014) and the results are presented in figure 4(*b*) for $We = 7.9$. Also in this case excellent agreement between simulation and experiment is observed.

For validation, simulations were performed within the experimentally accessed range of Weber numbers $6 < We < 25$. Dependence of characteristic times $t_{\uparrow}$, t_{max}, and $t_{contact}$ on Weber number is compared with the experiment in figure 5(*a*) (tapered posts) and figure 5(*b*) (square posts). Also the so-called pancake quality $Q = d_{jump}/d_{max}$ is compared to the experiment, where d_{jump} and d_{max} are the diameters of the drop at $t_{contact}$ and t_{max}, respectively.

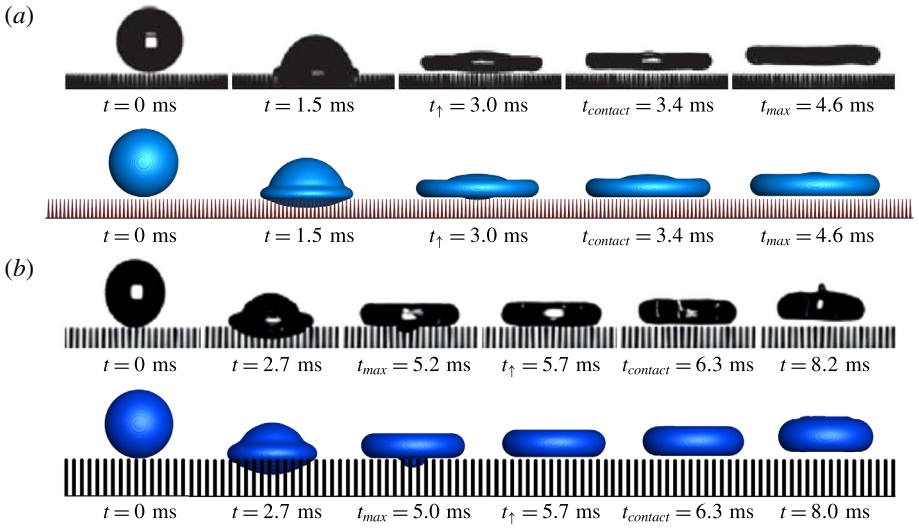

FIGURE 4. (Colour online) Comparison of simulation (bottom) and experiment (Liu *et al.* 2014) (top) for the pancake bouncing of a drop impinging on (*a*) the tapered posts at $We = 14.1$ and (*b*) the straight square posts at $We = 7.9$.

Simulations in figure 5(*a*) show that for $We < 12$ the contact time is $t_{contact} \simeq 16$ (ms) which is in good agreement with the conventional complete rebound from a flat surface (Richard *et al.* 2002). The onset of the pancake bouncing regime at critical Weber number $We^* \approx 12$ agrees well with experiment (Liu *et al.* 2014). Reduction in contact time by a factor four is observed. We repeated the measurements of the characteristic times scales for the drop impinging on the straight square posts. Simulation results compare well with the experiment in figure 5(*b*).

Summarizing, ELBM simulation demonstrates excellent agreement with the existing experimental data. In the remainder of this paper, we shall address regimes which were so far not studied experimentally in order to gain a more comprehensive picture of bouncing off macro-textured surfaces.

3.3. *Textures with perfect coating*

Liu *et al.* (2014) reported experiments in a narrow range of Weber numbers ($We < 25$). When the Weber number is increased, penetration depth into the texture increases and the deforming drop will eventually reach the base of the substrate. It is difficult to study the liquid inside the texture in the experiments. Here we extend the ELBM simulations to higher Weber numbers, $6 < We < 150$. We first consider the same geometry as in the previous section, and assume perfect coating, that is, both the posts and the base are SHS with contact angle $\theta = 165°$.

Figure 6 shows snapshots of the impact on the perfectly coated texture at various Weber numbers. For $We > 40$, the penetrated liquid interacts with the base plate at the time t_{mpl} (maximal penetration of the drop). Simulations show that pancake bouncing is still observed for a much wider range of Weber numbers, $12 < We < 150$. Figure 7 shows that both the reduction of the contact time (squares) and the pancake quality (circles) remain unaffected until at least $We \approx 150$. This can be attributed to the fact that the base plate of the texture is also considered an SHS with a uniform contact angle (see § 3.5).

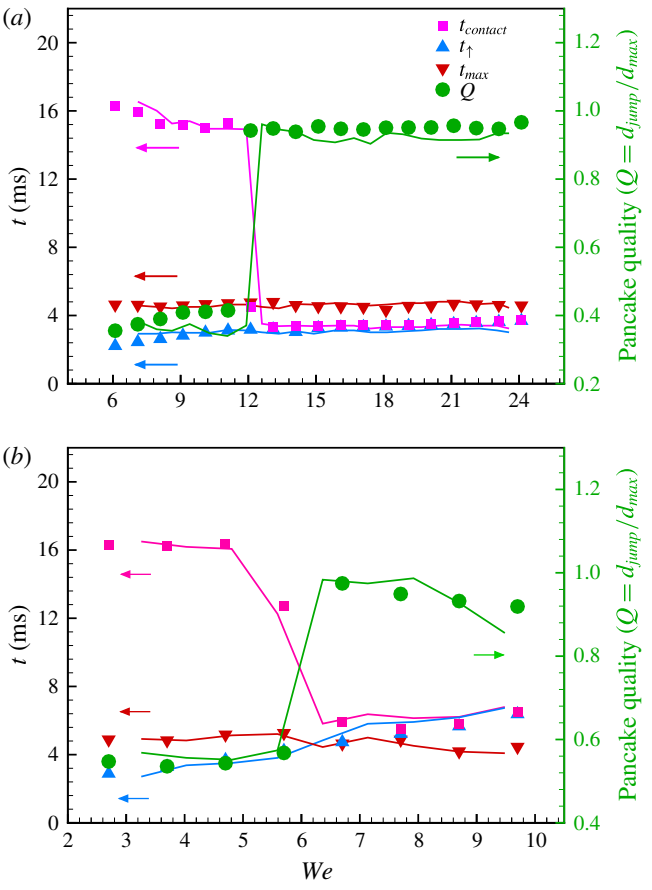

FIGURE 5. (Colour online) Drop rebound from macro-texture at various Weber numbers. Symbol: simulation; line: experiment (Liu *et al.* 2014). Characteristic times: $t_{\uparrow}$ (emptying time, blue), t_{max} (maximum lateral extension time, red), $t_{contact}$ (contact time, magenta); pancake quality $Q = d_{jump}/d_{max}$ (green) where d_{jump} and d_{max} are the diameters of the drop at $t_{contact}$ and t_{max}, respectively. (*a*) Tapered posts. Geometry of the posts used in the simulations matches the experiment: $R_0/h = 1.8$ (droplet radius to post height), density of texture $R_0/w \approx 7.25$ (droplet radius to centre-to-centre spacing), $b/B \approx 0.28$ (smaller to larger diameter of the bases) and $b = B - 2h \tan\varphi$ ($\varphi = 2.6°$ is the apex angle) (supplementary movies 2 and 3). (*b*) Square posts.

Summarizing, under the assumption of perfect SHS coating, we found that the pancake bouncing extends to much higher Weber numbers, with the critical Weber number clearly identified and in agreement with experimental observations.

3.4. *Critical Weber number and density of texture*

In the above simulations, the density of the texture, $\Lambda = R_0/w \approx 7.25$, matched the experiment (Liu *et al.* 2014) and the critical Weber number $We^* \approx 12$ at the onset of the contact time reduction was found in both simulation and experiment (see figures 5*a*, 7). Next we study the effect of density of the texture (DoT) $\Lambda = R_0/w$ on the contact time reduction by varying the centre-to-centre spacing w. Intuitively,

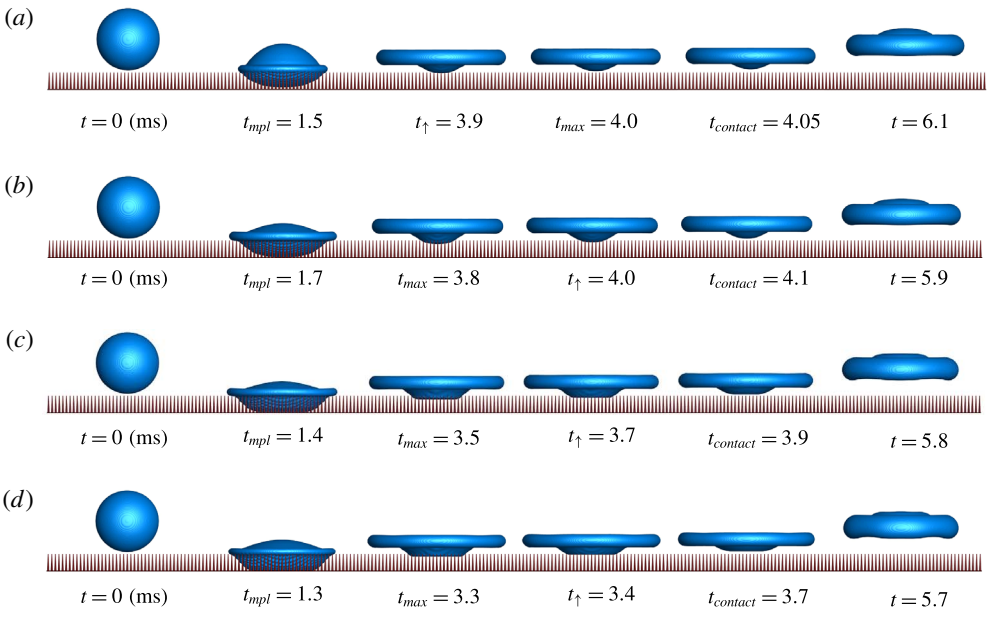

FIGURE 6. (Colour online) Snapshots of the rebound from tapered posts at (*a*) $We = 40$, (*b*) $We = 50$, (*c*) $We = 80$, (*d*) $We = 120$. Density of the texture $\Lambda_{exp} = 7.25$. Invading liquid hits the base of the texture at $We \geqslant 50$. Perfect coating is assumed for both the posts and the base plate (contact angle is set to $\theta = 165°$). After hitting the base, penetrated liquid experiences a quick lateral extension, detaches from the base, returns to the top of the posts and demonstrates pancake rebound (supplementary movies 4 and 5). Geometry of the macro-texture is same as in figure 5(*a*).

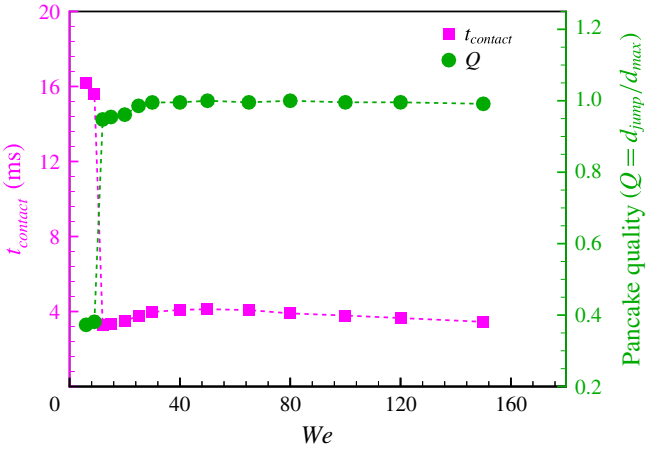

FIGURE 7. (Colour online) Contact time $t_{contact}$ (squares) and pancake quality Q (circles) of a drop impinging on perfectly coated tapered posts with the density of texture $\Lambda_{exp} = 7.25$, for a range $6 \leqslant We \leqslant 150$. Geometry of the macro-texture is same as in figure 5(*a*).

one expects the limit of contact time of the flat SHS to be reached for both sparse ($\Lambda \approx 1$) and dense textures ($\Lambda \gg 1$; in the present simulation, the maximal texture density is reached at $\Lambda \approx 12.5$ when the bases of the posts start to overlap). In the

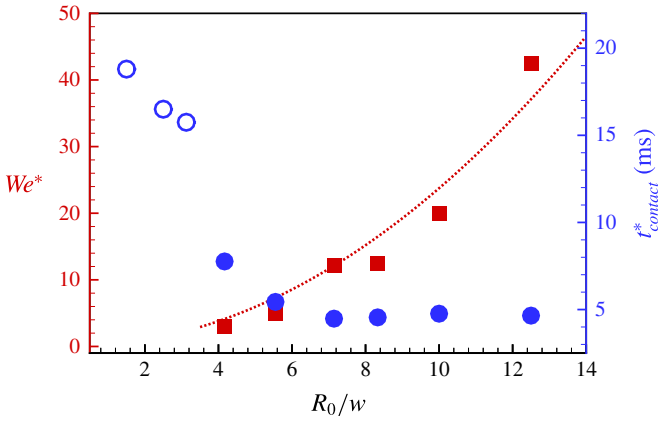

FIGURE 8. (Colour online) Square: dependence of the critical Weber number We^* on the density of texture $\Lambda = R_0/w$; Line: quadratic fit of the critical Weber number for the realizations between $\Lambda = 4$ and $\Lambda = 12.5$. Circle: contact time at We^* for the corresponding density of texture. Open symbols indicate that the critical Weber number was not observed for the corresponding density of texture. Various Λ were realized by changing the post's centre-to-centre spacing w under fixed drop radius R_0. At $\Lambda = 12.5$, the bases of the conical posts touch each other. Dimensions of the posts are same as in the experiment.

intermediate range, the critical Weber number We^* can be observed, at which the reduction of the rebound time occurs.

Figure 8 shows the dependence of the critical Weber number on the density of texture $We^*(\Lambda)$, and the corresponding contact time, $t^*(\Lambda) = t_{contact}(We^*(\Lambda))$. From figure 8, one can see that the critical Weber number and the associated contact time reduction is first found at $\Lambda = 4$ and extends to higher DoT. Note that, while We^* was found at DoT as high as $\Lambda \approx 12.5$ in the simulation, the corresponding value $We^*(12.5) \approx 42.5$ is far off the range of Weber numbers probed in the experiment ($We < 30$). In other words, if a limited range of Weber numbers is concerned, the case of very dense textures ($\Lambda = 12.5$ was the most dense texture in the simulation since the bases of the cones start to overlap) shows the limit of the flat SHS as the drop resists to penetrate into the texture.

A qualitative estimate of the dependence $We^*(\Lambda)$ can be based on the following arguments. First, we recall the explanation of contact time reduction on the macro-wedges in Gauthier *et al.* (2015). If the drop is deformed by the macro-structure in such a way that it can be represented by a partition into N smaller blobs, the inertia–capillary time $\tau \sim \sqrt{\rho R_0^3/\sigma}$ transforms to $\tau \sim \sqrt{\rho R_0^3/N\sigma}$, which explains the experimentally observed scaling of contact time reduction, $t_{contact} \sim N^{-1/2}$ (see Gauthier *et al.* 2015). In the present case, the 'blobs picture' pertains to the penetrated liquid. The number of blobs (liquid filaments invading the spacing between the posts) can be estimated as $N \sim \Lambda^2$, and thus the emptying time $t_\uparrow$ scales as $t_\uparrow \sim \sqrt{\rho R_0^3/\Lambda^2\sigma} \sim (R_0/U)\sqrt{We/\Lambda^2}$. Second, the spreading time of the part of the drop over the top of the texture $t_\rightarrow$ can be estimated by the crashing time (Clanet *et al.* 2004), $t_\rightarrow \sim R_0/U$, that is, it does not depend on DoT Λ. Finally, following the argument of Liu *et al.* (2014), at the critical Weber number, the spreading and the emptying times should match (see figure 5*a*), $t_\rightarrow \approx t_\uparrow$. Using the above estimates, we obtain $We^* \sim \Lambda^2$. Thus, the present simple arguments, although not universal, imply a

quadratic dependence of the critical Weber number on the density of texture, which is consistent with the simulation results in figure 8.

The blue circles in figure 8 shows the contact time as a function of DoT, measured at the critical Weber number for each Λ. The onset of contact time reduction is clearly visible at $\Lambda = 4$. Note that the critical $t^*(\Lambda)$ is confined to a band between a two to four times reduction with respect to the contact time of the flat SHS. In other words, while the contact time reduction may be not as significant for lower DoT as compared to the spectacular four times reduction at the close to optimal DoT $\Lambda \approx 7$ of the experiment (Liu *et al.* 2014), it is still clearly lower than the flat SHS values. In that respect, the blue circles in figure 8 are reminiscent of the 'quantization' of the contact time plots on the SHS wedge macro-structures (see figure 3*a* of Gauthier *et al.* 2015), with relatively narrow band of reduced contact times for a range of DoTs.

Summarizing, under the assumption of perfect SHS coating, we find that the density of the texture strongly affects the critical Weber number, with the transition to reduced contact time growing nonlinearly (quadratically) with DoT. Hence, during a design process, one needs to consider the trade-off between the amount of reduction in the contact time and the critical Weber number at which the contact time reduction sets in. Also, the observation of significant time reduction in a wide range of DoTs makes it possible to avoid the perfect arrangements of pillars. In the next section we shall investigate the effect of imperfect coating on the contact time reduction.

3.5. *Imperfect coating*

So far we have assumed that the SHS quality is maintained uniformly throughout the texture and the base plate. However, this is unlikely to hold when, for example, the SHS coating is produced by spraying a polymer solution on the texture. According to Liu *et al.* (2014), controlling the quality and uniformity of coating throughout the posts, and especially in the valleys between them, is a difficult task. Hence it is reasonable to assume that the contact angle at the base plate is lower than that on the upper part of the posts. Since the drop interacts with the base plate at $We \geqslant 50$ (see figure 6), we probe the effect of imperfect coating by assigning a smaller contact angle for the base plate and the bottom part of the posts (10 % of the height). Since SHS are usually manufactured by coating hydrophobic surfaces with nano-scale structures, we choose three different contact angles at the base plate and the bottom part of the posts, $\theta_{bottom} = 132^\circ$ ($\kappa_w = -0.09625$) (2.3), 140° ($\kappa_w = -0.105$) and 145° ($\kappa_w = -0.115$). These values are reasonable for conventional hydrophobic surfaces. The upper part the posts is maintained at the SHS contact angle $\theta = 165^\circ$ as before, and the density of texture is fixed at $\Lambda_{exp} = 7.25$.

Contact time for imperfectly coated textures is shown in figure 9. For $We \leqslant 40$, the contact time is the same for all coatings considered; since liquid penetrates the texture without touching the base, the quality of coating has no effect on the contact time. However, for $We > 40$, the liquid reaches the substrate base, and degraded coating alters significantly the contact time droplet dynamics and the pancake quality. As seen from figure 9, deterioration of the contact time becomes progressively more severe with lowering of the contact angle at the bottom, as expected. For the smallest contact angle $\theta_{bottom} = 132^\circ$, for $We > 40$, the impacting drop sticks to the substrate base. Consequently, the drop rebounds in a conventional fashion, with approximately the same contact time as for the flat SHS, in the entire range of Weber numbers $We = 65 - 150$. However, for a less severe degradation, $\theta_{bottom} = 140^\circ$ and 145°, we observe a nonlinear dependence of the contact time on the Weber number $We > 40$.

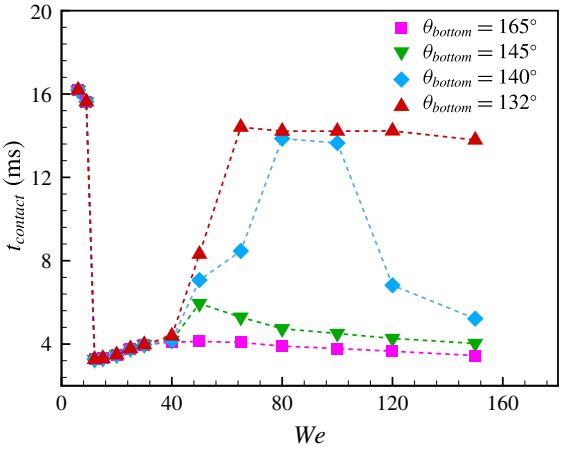

FIGURE 9. (Colour online) Contact time $t_{contact}$ (ms) for imperfectly coated textures at three different contact angles at the substrate base, $\theta_{bottom} = 145°$, $\theta_{bottom} = 140°$ and $\theta_{bottom} = 132°$, as a function of Weber number. Reference data for perfectly coated texture $\theta_{bottom} = 165°$ are also shown. Geometry of the texture is same as in figure 5(*a*).

In order to elucidate this nonlinearity, in figure 10 we present snapshots of the impact for $\theta_{bottom} = 140°$, for different Weber numbers. For $We = 50$, 80 and 120, the drop contacts with the substrate base at t_{mpl}. Due to lack of superhydrophobicity at the bottom, the penetrated liquid tends to stick to the texture base before it is pulled out by the rest of drop moving upward. In figure 10(*b*) ($We = 50$), although the penetrated liquid sticks to the substrate base, it returns to the top of the texture quickly thus enabling pancake bouncing but with an almost double contact time, $t_{contact} \approx 7$ (ms). At a higher Weber number $We = 80$, figure 10(*c*), due to a larger contact area between the liquid and the texture base, the penetrated liquid returns to the top of the posts with a delay. Consequently, the drop has enough time to retract and the overall picture resembles the conventional bouncing rather than a pancake rebound. The contact time $t_{contact} \approx 14$ (ms) becomes closer to the conventional bouncing value (see Supplementary Movie 6). However, as the Weber number is further increased, figure 10(*d*), $We = 120$, the contact time reduces back to the value $t_{contact} \approx 7$ (ms). In this case, since the contact area between the drop and the base becomes even larger, also the number of invaded valleys increases. The force due to surface tension is thus able to overcome the pinning effect of the imperfectly coated base and the texture is emptied faster. This explains the return of a pancake-like bouncing at $We = 120$, and the contact time becomes smaller than at $We = 80$.

Summarizing, a moderately degraded coating at the bottom of the texture features a nonlinear dependence of the contact time on the Weber number and significantly affects the rebound pattern.

3.6. *Energy budget*

Energy considerations were invoked in Liu *et al.* (2014) to quantify the mechanism of pancake bouncing. The assumption behind this analysis was that the kinetic energy of the drop is fully converted into the surface energy at the maximal penetration into the texture. However, neglecting energy dissipation is less obvious for an impact on textured surfaces. Indeed, since the shape of the droplet is considerably more distorted

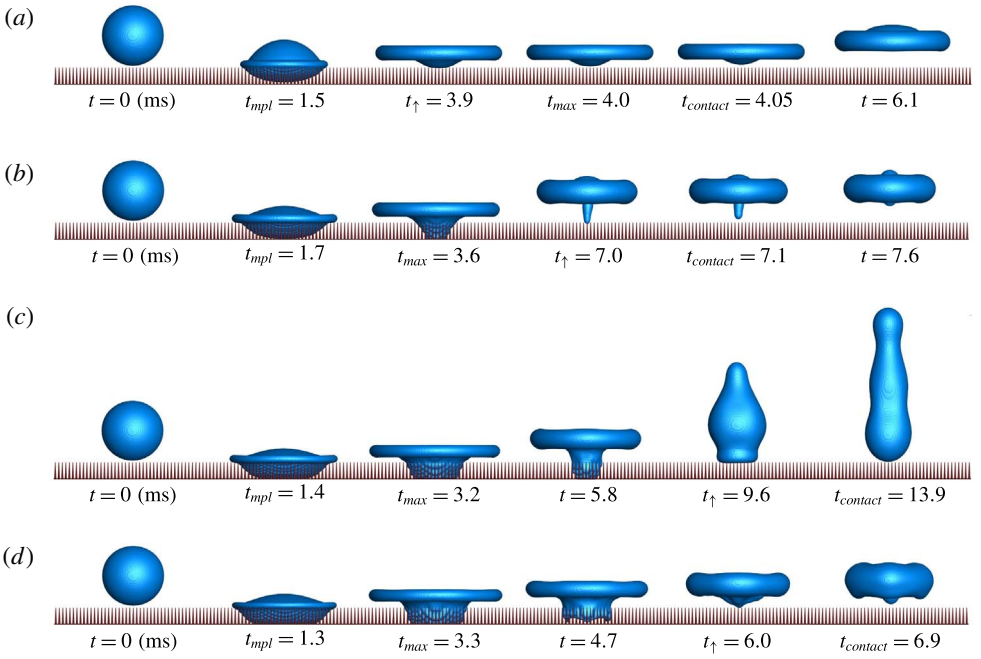

FIGURE 10. (Colour online) Snapshots of impact on imperfectly coated texture at (*a*) $We = 40$, (*b*) $We = 50$, (*c*) $We = 80$, (*d*) $We = 120$. Contact angle at the base plate and 10 % above it set to $\theta_{bottom} = 140°$, and for the rest of the texture the contact angle is $\theta = 165°$. For $We \geqslant 50$, the penetrated liquid reaches the base at t_{mpl}. Geometry of the macro-texture is same as in figure 5(*a*). (Supplementary Movies 6 and 7.)

as compared to the flat SHS (the flow 'sees more walls'), stresses in the boundary layers contribute more to the dissipation. On the other hand, ELBM was shown to quantitatively capture the energy budget in binary droplet collisions (Mazloomi Moqaddam *et al.* 2016). In this section we report and discuss the energy budget of the pancake bouncing regime from the ELBM simulations. For a drop with volume V and surface area A, let us introduce the kinetic energy, $K = \int_V (\rho u^2 \, \mathrm{d}V)/2$, the surface energy $S = \sigma A$ and the energy loss due to viscous dissipation Ξ,

$$\Xi = \int_0^t \Phi \, \mathrm{d}t \quad \text{where } \Phi = \frac{\mu_l}{2} \int_V (\boldsymbol{\nabla u} + \boldsymbol{\nabla u}^{\dagger})^2 \, \mathrm{d}V. \tag{3.1}$$

Further introducing normalized energies, $\tilde{K} = K/E_0$, $\tilde{S} = S/E_0$ and $\tilde{\Xi} = \Xi/E_0$, where $E_0 = K_0 + S_0$ is the energy of the drop at $t = 0$, the energy balance is written as,

$$\tilde{K} + \tilde{S} + \tilde{\Xi} = 1. \tag{3.2}$$

All three components of the energy balance equation (3.2) were evaluated individually for the impact on a perfectly coated texture with the texture density $\Lambda_{exp} = 7.25$ (§§ 3.2 and 3.3). In figure 11 we present the time evolution of $\tilde{K}$, $\tilde{S}$ and $\tilde{\Xi}$. We also show the normalized centre-of-mass kinetic energy $\tilde{K}_{cm} = K_{cm}/E_0$ where $K_{cm} = (mU_{cm}^2)/2$ is the kinetic energy of centre-of-mass, with m the mass of the liquid and U_{cm} the centre-of-mass velocity. Results for three representative

We	$\tilde{K}_0^{exact}$	$\tilde{K}_0^{num}$	$\tilde{S}_0^{exact}$	$\tilde{S}_0^{num}$
15	0.714	0.712	0.286	0.287
30	0.833	0.835	0.167	0.164
80	0.930	0.926	0.07	0.075

TABLE 1. Reduced kinetic and surface energy for the spherical drop.

Weber numbers are shown: $We = 15$ (shortly after the onset of pancake bouncing at $We^* \approx 12$); $We = 30$ (at the limit of the experimentally accessed Weber numbers; significant intrusion of liquid into the texture) and $We = 80$ (large intrusion).

Before discussing the results, a brief comment on the validation of the numerics is in order. First, the numerical result at $t = 0$ (spherical unperturbed drop moving with the velocity U_0) satisfies well the exact relations, $\tilde{K}_0 = We/(We + 6)$, $\tilde{S}_0 = 6/(We + 6)$; see table 1. Also, the energy balance (3.2) is satisfied within 2 % for all times and Weber numbers which is consistent within the accuracy of evaluation of velocity gradients in the computation of energy dissipation.

The first observation concerns the kinetic energy $\tilde{K}$ and the centre-of-mass kinetic energy $\tilde{K}_{cm}$. While the latter vanishes at the maximal penetration of the drop into the texture, the kinetic energy itself is different from $\tilde{K}_{cm}$. This difference is attributed to the flow inside the rim of the upper part of the drop remaining on top of posts as well as the opposing flow directions observed inside the droplet. Flow inside the deformed droplet is visualized by snapshots of velocity field in figure 12. The non-negligible amount of kinetic energy carried by the flow of this type was indicated in Clanet *et al.* (2004) for drop impact on a flat surface. With the increase of Weber number, a greater part of the droplet penetrates the texture, hence the amount of energy carried by this flow decreases. This is consistent with the result of simulation which shows that the relative difference between $\tilde{K}$ and $\tilde{K}_{cm}$ decreases with the Weber number.

Second, the surface energy $\tilde{S}$ rapidly increases after the impact, as expected. For $We = 15$ we see two maxima of $\tilde{S}$, a local maximum close to the zero of the centre-of-mass velocity (the drop has stopped penetrating into the texture) and then the global maximum at the time of maximum lateral extension. Note that in this case, maximal extension comes after the droplet bounces off the texture. However, with the increase of the Weber number, the second maximum tends to disappear and is not present at $We = 80$. This situation can be termed a pseudo-pancake rebound in order to distinguish it from the true rebound at $We = 15$: the maximal stretching synchronizes with the maximum penetration time and does not affect the contact time, as was shown above.

Finally, it is clear from the energy balance at all Weber numbers that the dissipation is not negligible in any of the cases for the simulated Ohnesorge number $Oh = 0.025$. While for the lower $We = 15$, the surface energy becomes dominant soon after the impact, dissipation is not small even in that case with levels around 25 % at the rebound. It is seen from figure 11 the fraction of energy loss at higher Weber numbers is even larger and dominates others at $We = 80$.

Liu *et al.* (2015*b*) discussed a possibility that macroscopic air pockets get trapped between the droplet and the substrate. Such trapped pockets of air or vapour can undergo compression which could serve as an additional storage of energy to be released into the kinetic energy during the capillary emptying. However, the energy balance evaluation above suggests that such a scenario need not be present.

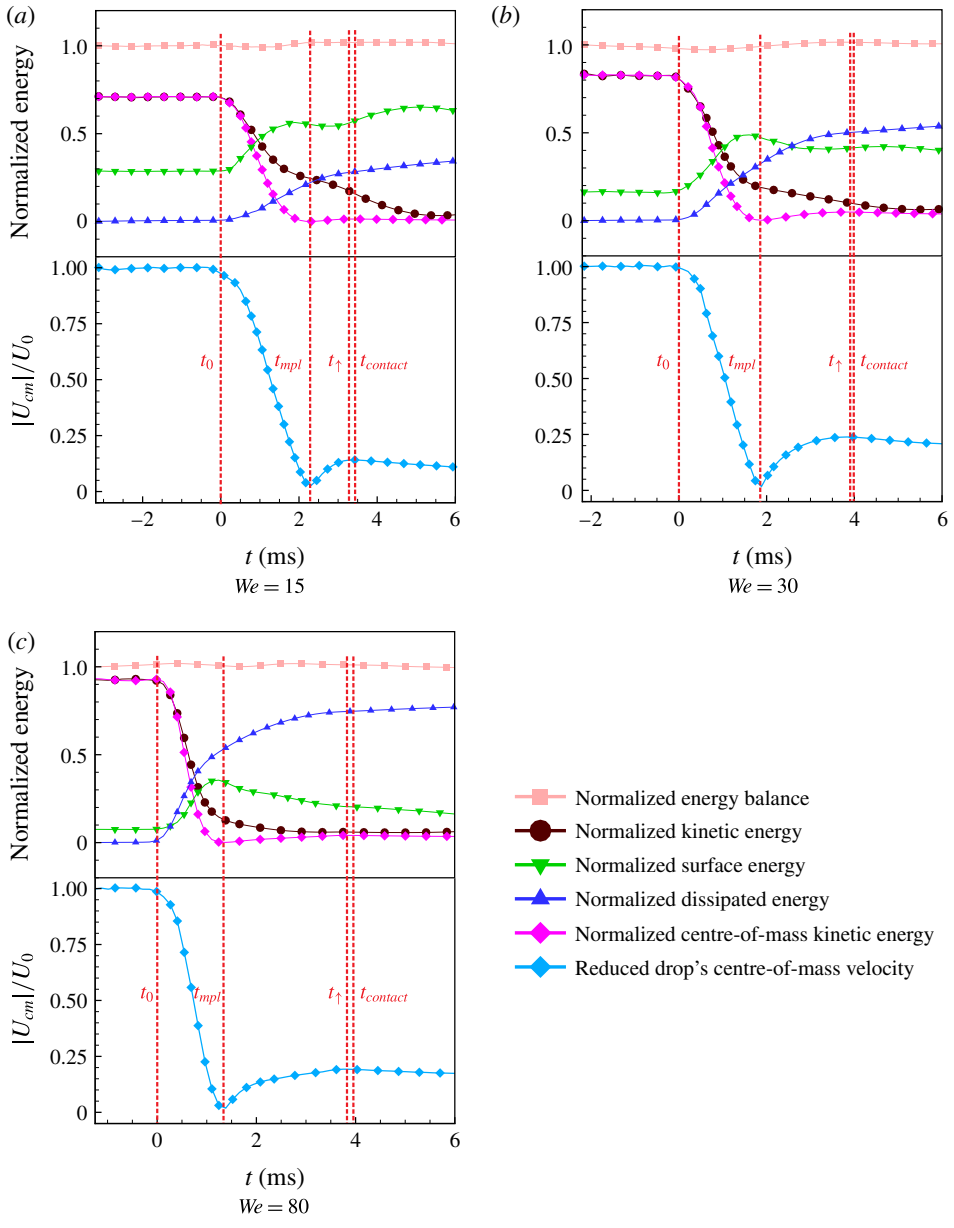

FIGURE 11. (Colour online) (*a*,*b*) History of various components of the energy balance. Circles: normalized kinetic energy $\tilde{K}$; downward triangles: normalized surface energy $\tilde{S}$; upward triangles: normalized dissipated energy $\tilde{\Xi}$. Squares: normalized energy balance $\tilde{K} + \tilde{S} + \tilde{\Xi}$. Diamonds: normalized centre-of-mass kinetic energy $\tilde{K}_{cm}$. (*c*) Reduced centre-of-mass velocity of the drop U_{cm}/U_0. Impact on a perfectly coated SHS $\theta = 165°$ for low and high Weber numbers (supplementary movie 8).

Summarizing, for the macroscopically flat superhydrophobic surface, the scaling of the contact time holds whenever the Ohnesorge number is not too large ($Oh < 1$) (Antonini *et al.* 2016). Similar universality holds also in the case of tapered

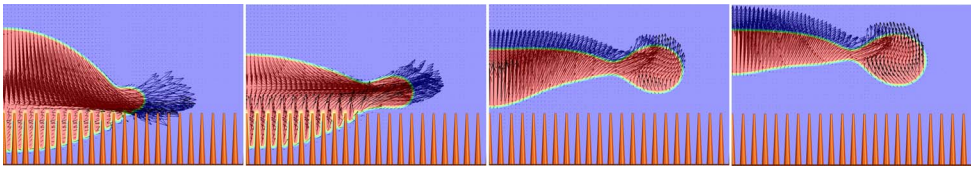

FIGURE 12. (Colour online) Visualization of the velocity vectors inside the middle plane of the drop impacting on the tapered posts for different times, $We = 30$.

macro-texture: while the dissipation is not necessarily negligible for $Oh = 0.025$, the contact time of the pancake bouncing scales the same way as in the experiment with water droplets. The only important requirement for that mechanism to be realized is the clear dominance of the surface energy over the kinetic energy at the instance of maximal penetration into the texture. Thus, such energy balance analysis could be very handy in estimating the role played by kinetic, surface and viscous forces for a droplet–wall interaction. Such analysis is of greater use when the underlying mechanisms of droplet bouncing are not well understood, for example complex macro-textured surfaces. Moreover, imbalance in energy analysis could lead to a better understanding of the role played by external factors such as trapped air pockets, thus enabling the design and optimization of novel surface textures. However, the study of the compressibility effects due to presences of the air pockets is not within the scope of this paper. Indeed, full access to compressibility effects requires a viable compressible flow lattice Boltzmann (LB) model and thus further advancements are required to extend the present quasi-incompressible LB model to capture these effects. A reliable compressible LB model for single-phase flows was recently introduced in (Frapolli, Chikatamarla & Karlin 2015, 2016) and incorporation of this model into the multiphase/multicomponent setting should be the subject of future work.

3.7. *Impact on a tilted macro-texture*

Finally, we apply our model to capture the impact of a drop on tilted macro-textured surface. Figure 13 demonstrates that pancake bouncing takes place also for the surface tilted at $\phi = 30°$. Both the snapshots and the contact time $t_{contact} = 3.6$ (ms) for the situation shown in figure 13 are in good agreement with those observed in the experiment (Liu *et al.* 2014). Figure 14 reports the contact time for an inclined surface for different tilt angles in a range of Weber numbers from $We = 6$ to $We = 150$. From figure 14, at a tilt angle of $\phi = 30°$, the pancake bouncing sets in at $We \geqslant 25$, that is, at an almost twice as high Weber number as compared to the normal impact ($\phi = 0°$). This happens since the motion along the slope delays the penetration of the liquid into the texture. It is also noted that by increasing the inclination angle, the transition to the pancake bouncing is more gradual than a sharp transition observed for the horizontally aligned substrate.

4. Conclusions

The dynamic behaviour of a liquid drop impacting a surface with tapered posts was numerically investigated over a wide range of Weber numbers using two-phase entropic lattice Boltzmann method. Superior stability of the ELBM and the flexibility

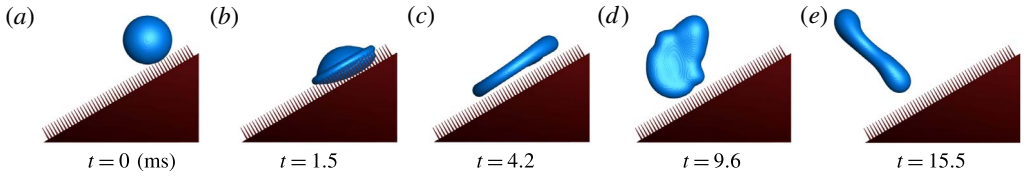

FIGURE 13. (Colour online) Snapshots of an impact on tapered posts tilted at $\phi = 30°$; $We = 31.2$. The drop rebounds at $t_{contact} = 3.6$ (ms) which is in excellent agreement with the experiment (Liu *et al.* 2014). Snapshots correspond to figure 1(*d*) of Liu *et al.* (2014) (supplementary movie 9).

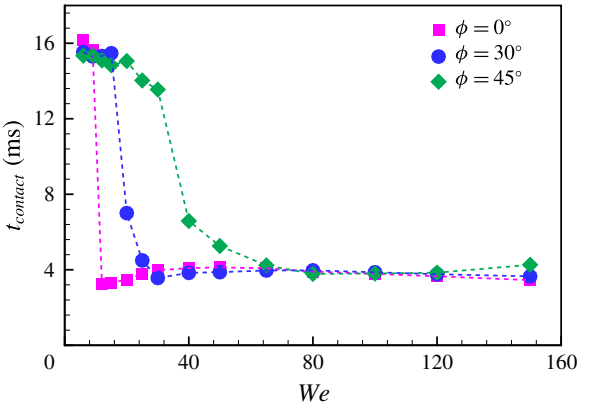

FIGURE 14. (Colour online) Contact time of a liquid drop impinging on tapered surface for two tilt angles, $\phi = 30°$ and $\phi = 45°$ in a range of Weber numbers, $6 \leqslant We \leqslant 150$. Reference data for the normal impact, $\phi = 0°$ are also shown. Significant reduction in the contact time occurs at larger Weber numbers by increasing the tilt angle.

of the wall boundary conditions allow us to study, for the first time, the pancake bouncing phenomenon in detail. Quantitative comparisons of ELBM simulations with previous experiments demonstrate the predictive nature of the multiphase entropic lattice Boltzmann model (Mazloomi Moqaddam *et al.* 2015*b*).

Apart from varying the surface parameters such as the spacing between posts and contact angle, this simulation technique allows us to accurately account for the transformation of kinetic energy into surface energy and *vice versa*. We presented numerical evidence that reduction in contact time occurs entirely due to increase of droplet surface area which acts as a storage of kinetic energy during the impact process. Such energy balance analysis, for the first time, allows us to accurately design and optimize surfaces and to understand the role played by various physical phenomena involved in droplet–wall interactions. Furthermore the impact of a surface superhydrophobic coating can be quantitatively accessed through numerical simulations.

Acknowledgements

This work was supported by the European Research Council (ERC) Advanced Grant 291094-ELBM, the ETH Research Grant ETH35-12-2 and the Swiss National Science

Foundation Grant 200021-172640/1. Computational resources at the Swiss National Super Computing Center CSCS were provided under the grant s492 and s630.

Supplementary movies

Supplementary movies are available at https://doi.org/10.1017/jfm.2017.306.

REFERENCES

ANSUMALI, S., KARLIN, I. V. & ÖTTINGER, H. C. 2003 Minimal entropic kinetic models for hydrodynamics. *Europhys. Lett.* **63** (6), 798.

ANTONINI, C., BERNAGOZZI, I., JUNG, S., POULIKAKOS, D. & MARENGO, M. 2013*a* Water drops dancing on ice: how sublimation leads to drop rebound. *Phys. Rev. Lett.* **111** (1), 014501.

ANTONINI, C., JUNG, S., WETZEL, A., HEER, E., SCHOCH, P., MAZLOOMI MOQADDAM, A., CHIKATAMARLA, S. S., KARLIN, I., MARENGO, M. & POULIKAKOS, D. 2016 Contactless prompt tumbling rebound of drops from a sublimating slope. *Phys. Rev. Fluids* **1** (1), 013903.

ANTONINI, C., VILLA, F., BERNAGOZZI, I., AMIRFAZLI, A. & MARENGO, M. 2013*b* Drop rebound after impact: the role of the receding contact angle. *Langmuir* **29** (52), 16045–16050.

BIANCE, A.-L., CLANET, C. & QUÉRÉ, D. 2003 Leidenfrost drops. *Phys. Fluids* **15** (6), 1632–1637.

BIRD, J. C., DHIMAN, R., KWON, H.-M. & VARANASI, K. K. 2013 Reducing the contact time of a bouncing drop. *Nature* **503** (7476), 385–388.

BLOSSEY, R. 2003 Self-cleaning surfaces – virtual realities. *Nat. Mater.* **2** (5), 301–306.

CHIKATAMARLA, S. S., ANSUMALI, S. & KARLIN, I. V. 2006 Entropic lattice boltzmann models for hydrodynamics in three dimensions. *Phys. Rev. Lett.* **97** (1), 010201.

CLANET, C., BÉGUIN, C., RICHARD, D. & QUÉRÉ, D. 2004 Maximal deformation of an impacting drop. *J. Fluid Mech.* **517**, 199–208.

DE RUITER, J., LAGRAAUW, R., VAN DEN ENDE, D. & MUGELE, F. 2015 Wettability-independent bouncing on flat surfaces mediated by thin air films. *Nat. Phys.* **11** (1), 48–53.

FRAPOLLI, N., CHIKATAMARLA, S. S. & KARLIN, I. V. 2015 Entropic lattice boltzmann model for compressible flows. *Phys. Rev.* E **92** (6), 061301.

FRAPOLLI, N., CHIKATAMARLA, S. S. & KARLIN, I. V. 2016 Lattice kinetic theory in a comoving galilean reference frame. *Phys. Rev. Lett.* **117** (1), 010604.

GAUTHIER, A., SYMON, S., CLANET, C. & QUÉRÉ, D. 2015 Water impacting on superhydrophobic macrotextures. *Nat. Commun.* **6**, 8001.

JUNG, S., TIWARI, M. K., DOAN, N. V. & POULIKAKOS, D. 2012 Mechanism of supercooled droplet freezing on surfaces. *Nat. Commun.* **3**, 615.

KARLIN, I. V., FERRANTE, A. & ÖTTINGER, H. C. 1999 Perfect entropy functions of the lattice Boltzmann method. *Europhys. Lett.* **47** (2), 182.

KOLINSKI, J. M., RUBINSTEIN, S. M., MANDRE, S., BRENNER, M. P., WEITZ, D. A. & MAHADEVAN, L. 2012 Skating on a film of air: drops impacting on a surface. *Phys. Rev. Lett.* **108** (7), 074503.

KORTEWEG, D. J. 1901 Sur la forme que prennent les equations du mouvements des fluides si lon tient compte des forces capillaires causes par des variations de densite. *Arch. Neerl. Sci. Exactes Nat. Ser.* II **6**, 1–24.

LIU, Y., ANDREW, M., LI, J., YEOMANS, J. M. & WANG, Z. 2015*a* Symmetry breaking in drop bouncing on curved surfaces. *Nat. Commun.* **6**, 10034.

LIU, Y., MOEVIUS, L., XU, X., QIAN, T., YEOMANS, J. M. & WANG, Z. 2014 Pancake bouncing on superhydrophobic surfaces. *Nat. Phys.* **10**, 515–519.

LIU, Y., WHYMAN, G., BORMASHENKO, E., HAO, C. & WANG, Z. 2015*b* Controlling drop bouncing using surfaces with gradient features. *Appl. Phys. Lett.* **107** (5), 051604.

MAITRA, T., ANTONINI, C., TIWARI, M. K., MULARCZYK, A., IMERI, Z., SCHOCH, P. & POULIKAKOS, D. 2014 Supercooled water drops impacting superhydrophobic textures. *Langmuir* **30** (36), 10855–10861.

MANDRE, S. & BRENNER, M. P. 2012 The mechanism of a splash on a dry solid surface. *J. Fluid Mech.* **690**, 148.

MANI, M., MANDRE, S. & BRENNER, M. P. 2010 Events before droplet splashing on a solid surface. *J. Fluid Mech.* **647**, 163.

MAZLOOMI MOQADDAM, A., CHIKATAMARLA, S. S. & KARLIN, I. V. 2015*a* Simulation of droplets collisions using two-phase entropic lattice boltzmann method. *J. Stat. Phys.* **161** (6), 1420–1433.

MAZLOOMI MOQADDAM, A., CHIKATAMARLA, S. S. & KARLIN, I. V. 2015*b* Entropic lattice boltzmann method for multiphase flows. *Phys. Rev. Lett.* **114**, 174502.

MAZLOOMI MOQADDAM, A., CHIKATAMARLA, S. S. & KARLIN, I. V. 2015*c* Entropic lattice boltzmann method for multiphase flows: fluid-solid interfaces. *Phys. Rev.* E **92**, 023308.

MAZLOOMI MOQADDAM, A., CHIKATAMARLA, S. S. & KARLIN, I. V. 2016 Simulation of binary droplet collisions with the entropic lattice boltzmann method. *Phys. Fluids* **28** (2), 022106.

MOEVIUS, L., LIU, Y., WANG, Z. & YEOMANS, J. M. 2014 Pancake bouncing: simulations and theory and experimental verification. *Langmuir* **30** (43), 13021–13032.

OKUMURA, K., CHEVY, F., RICHARD, D., QUÉRÉ, D. & CLANET, C. 2003 Water spring: a model for bouncing drops. *Europhys. Lett.* **62** (2), 237.

REIN, M. 1993 Phenomena of liquid drop impact on solid and liquid surfaces. *Fluid Dyn. Res.* **12** (2), 61.

RIBOUX, G. & GORDILLO, J. M. 2014 Experiments of drops impacting a smooth solid surface: a model of the critical impact speed for drop splashing. *Phys. Rev. Lett.* **113** (2), 024507.

RICHARD, D., CLANET, C. & QUÉRÉ, D. 2002 Surface phenomena: contact time of a bouncing drop. *Nature* **417** (6891), 811–811.

RICHARD, D. & QUÉRÉ, D. 2000 Bouncing water drops. *Europhys. Lett.* **50** (6), 769.

ROISMAN, I. V. 2009 Inertia dominated drop collisions. II. An analytical solution of the Navier–Stokes equations for a spreading viscous film. *Phys. Fluids* **21** (5), 052104.

ROISMAN, I. V., BERBEROVIĆ, E. & TROPEA, C. 2009 Inertia dominated drop collisions. I. On the universal flow in the lamella. *Phys. Fluids* **21** (5), 052103.

ROWLINSON, J. S. & WIDOM, B. 1982 *Molecular Theory of Capillarity*. Clarendon.

RYKACZEWSKI, K., LANDIN, T., WALKER, M. L., SCOTT, J. H. J. & VARANASI, K. K. 2012 Direct imaging of complex nano- to microscale interfaces involving solid, liquid, and gas phases. *ACS Nano* **6** (10), 9326–9334.

SCHUTZIUS, T. M., JUNG, S., MAITRA, T., GRAEBER, G., KÖHME, M. & POULIKAKOS, D. 2015 Spontaneous droplet trampolining on rigid superhydrophobic surfaces. *Nature* **527** (7576), 82–85.

TRAN, T., STAAT, H. J. J., PROSPERETTI, A., SUN, C. & LOHSE, D. 2012 Drop impact on superheated surfaces. *Phys. Rev. Lett.* **108** (3), 036101.

TRAN, T., STAAT, H. J. J., SUSARREY-ARCE, A., FOERTSCH, T. C., VAN HOUSELT, A., GARDENIERS, H. J. G. E., PROSPERETTI, A., LOHSE, D. & SUN, C. 2013 Droplet impact on superheated micro-structured surfaces. *Soft Matt.* **9** (12), 3272–3282.

TUTEJA, A., CHOI, W., MA, M., MABRY, J. M., MAZZELLA, S. A., RUTLEDGE, G. C., MCKINLEY, G. H. & COHEN, R. E. 2007 Designing superoleophobic surfaces. *Science* **318** (5856), 1618–1622.

WACHTERS, L. H. J. & WESTERLING, N. A. J. 1966 The heat transfer from a hot wall to impinging water drops in the spheroidal state. *Chem. Engng Sci.* **21** (11), 1047–1056.

WANG, Z., LOPEZ, C., HIRSA, A. & KORATKAR, N. 2007 Impact dynamics and rebound of water droplets on superhydrophobic carbon nanotube arrays. *Appl. Phys. Lett.* **91** (2), 023105.

XU, L. 2007 Liquid drop splashing on smooth, rough, and textured surfaces. *Phys. Rev.* E **75** (5), 056316.

XU, L., ZHANG, W. W. & NAGEL, S. R. 2005 Drop splashing on a dry smooth surface. *Phys. Rev. Lett.* **94** (18), 184505.

YARIN, A. L. 2006 Drop impact dynamics: splashing, spreading, receding, bouncing. *Annu. Rev. Fluid Mech.* **38**, 159–192.

YUAN, P. & SCHAEFER, L. 2006 Equations of state in a lattice boltzmann model. *Phys. Fluids* **18** (4), 042101.